Research Article Vol. 62, No. 20 / 10 July 2023 / Applied Optics 5565

applied optics

Composite scanning mechanism based on an aperiodic optical phased array

KUNYANG DU,[1,2] RUI WANG,[1,*] JIN GUO,[1] AND YUANYANG LI[1]

[1]State Key Laboratory of Laser Interaction with Matter, Changchun Institute of Optics, Fine Mechanics and Physics, Chinese Academy of Sciences, Changchun, 130033, China
[2]University of Chinese Academy of Sciences, Beijing, 100049, China
*darui9999@163.com

Received 1 May 2023; revised 15 June 2023; accepted 19 June 2023; posted 20 June 2023; published 7 July 2023

A composite scanning mechanism is proposed based on an aperiodic optical phased array (OPA). The OPA of this scheme has a two-stage scanning mode of sub-aperture multi-beam and single-beam high-resolution scanning. The scanning mode can be adaptively switched according to different environmental conditions. While retaining the advantages of high-speed and multi-target detection of sub-aperture multi-beam steering, a high-resolution scanning of the region of interest is realized. Simultaneously, the array distribution of the phased array is optimized using the adaptive-reference-point-based multi-objective evolutionary algorithm to reduce the grating lobe. The research conducted provides ideas for OPAs in practical applications.

https://doi.org/10.1364/AO.494513

1. INTRODUCTION

The light detection and ranging (LiDAR) system is a laser-based imaging technology for precise distance measurement. It is a core sensor technology for highly intelligent systems such as autonomous driving, unmanned aerial vehicles, and the Internet of Things, and has received wide attention [1,2]. The current mainstream LiDAR regime involves mechanical scanning, which is plagued by slow scanning speeds, large size, and mechanical wear and tear, thereby limiting its feasibility in certain application fields. In contrast, a solid-state lidar system with a silicon-based optical phased array (OPA) chip as the core adopts the chip-level solution of the silicon platform to replace the original relatively complex mechanical rotation structure. It can realize a wide range of high-precision pointing controls of the beam through electronic scanning. In addition, it is compatible with the mature complementary metal oxide semiconductor (CMOS) process and is suitable for mass production and integration, which is generally considered by the industry as the mainstream development direction in the future LiDAR field.

In recent years, there have been many reports on OPAs [3–5], and the great potential for OPA applications has been demonstrated in optical communication [6], ranging [7], indoor optical wireless communication [8], and special beam generation [9]. The current research mainly focuses on improving the overall performance of OPA, and has not conducted in-depth discussions on the flexible multi-beam modulation ability of OPA. However, the actual application scenarios are complex and variable, and a single beam cannot meet the application requirements. The ability of OPA to freely adjust the number and resolution of beams based on environmental changes is highly attractive. For example, in the field of autonomous driving, adaptive resolution can be realized according to the different surrounding environments, and in the application of indoor optical wireless communication, it can provide services for multiple users in different locations at the same time. In addition, the principle of OPA is the coherent diffraction of light [10]. Owing to the manufacturing level, the array element spacing is larger than half the wavelength ($\lambda = 1550$ nm). Therefore, the far field generates grating lobes, affecting the free adjustment ability of multi-beam. Most currently used methods for suppressing grating lobes involve unequally spaced arrays, which destroy the coherence condition of gating lobes by changing the array element spacing [11–13]. But these techniques are array optimized only for the case of single-stage beam scanning [14–16]. When performing free regulation of multiple beams, the performance of OPA will inevitably decrease. Therefore, the difficulty of OPA-based multi-stage beam modulation is to ensure the performance of OPA when the beam mode is switched.

This study proposes a composite scanning technology based on an aperiodic OPA. The OPA of this scheme involved a two-stage scanning mode of sub-aperture multi-beam and single-beam high-resolution scanning. The scanning mode can achieve adaptive switching according to different environmental conditions, and can quickly scan simple objects in the environment and obtain the details of complex objects. This scheme demonstrates the potential of OPA to achieve multi-stage beam switching. To ensure the stability of the performance

and suppress the grating lobe when the scanning mode is switched, the adaptive-reference-point-based multi-objective evolutionary algorithm (AR-MOEA) is used to optimize the sub-array and full-aperture distribution of the phased array. The performance of the OPA is analyzed through a numerical simulation.

2. PRINCIPLE

The typical one-dimensional OPA model is shown in Fig. 1. Considering a linear uniform array with N elements and assuming that the physical dimension of the optical antenna is ignored, the far-field distribution function $E(\theta)$ of this OPA can be expressed as [17]

$$E(\theta) = f(\theta)\sum_{i=1}^{N} A_i e^{j\left(\frac{2\pi}{\lambda} id\sin\theta - \Delta\varphi\right)}$$

$$\Delta\varphi = \frac{2\pi}{\lambda} id\sin\theta_s, \tag{1}$$

where $f(\theta)$ is the form factor of a single antenna unit, and the remaining are the array factors. Ai, λ, d, θ, and θs denote the amplitude of the light emitted by the ith element, optical wavelength, array spacing, observation direction, and beam scanning angle, respectively. When $\theta = \theta s$, the value of this function reaches its peak; that is, the beam direction of the array antenna is θs. Therefore, by setting different progressive phase shifts, $\Delta\varphi$, the beam can be steered in different directions. In the following simulation process, to simplify the analysis, the form factor of the array element is assumed to be isotropic ($f(\theta) = 1$), and the amplitude intensity of the light from each array element is equal ($Ai = 1$). The far-field light intensity can be expressed as

$$I(\theta) = |E(\theta)|^2 = \frac{\sin^2\left[N\frac{\pi}{\lambda}d\left(\sin\theta - \sin\theta_s\right)\right]}{\sin^2\left[\frac{\pi}{\lambda}d\left(\sin\theta - \sin\theta_s\right)\right]}. \tag{2}$$

Theoretically, the steering range of the OPA is limited by at least two factors: aliasing and diffraction envelope. Aliasing is the higher-order interference other than the main direction. The diffraction envelope is the far-field diffraction angle range of a single antenna, which is not considered here. The position of grating lobes of a single beam are determined by

$$\theta_m = \pm\arcsin\left(\frac{m\lambda}{d} + \sin\theta_s\right), \quad m = 1, 2, 3\ldots, \tag{3}$$

where m denotes the order of grating lobes, as shown in Fig. 2. Therefore, the grating lobe is mainly affected by the spacing between antennas.

Beam width is an index of phased array angle resolution, which is closely related to scanning accuracy. In this paper, the beam width is defined as the full width at half maximum (FWHM) of the main beam:

$$\mathrm{FWHM} \approx \frac{0.886\lambda}{Nd\cos\theta_s}. \tag{4}$$

As evident from the above equation, the beam FWHM is inversely proportional to the array aperture A (A = Nd); that is, the larger the aperture, the smaller the beam FWHM and the higher the beam angular resolution.

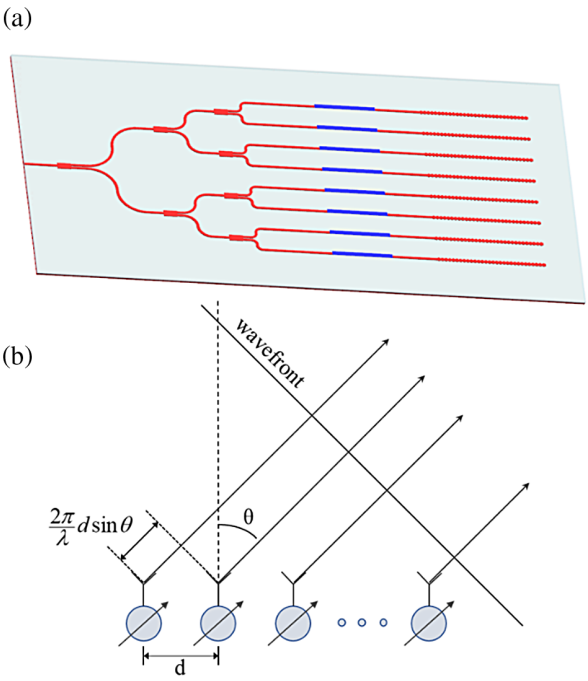

Fig. 1. (a) Structure diagram of one-dimensional OPA; (b) illustration of one-dimensional linear phased array.

Now we consider the compound-scanning scheme, as shown in Fig. 3. The sub-aperture technology in Fig. 3(a) divides the OPA array of N elements into M sub-arrays, and the sub-arrays are separately modulated to achieve the independent scanning of multiple beams. Assuming that the sub-aperture array has m elements and that the element spacing d is equal, the far-field distribution function of the OPA can be expressed as

$$\begin{aligned} E(\theta) &= \sum_{n=1}^{N} e^{jnd\frac{2\pi}{\lambda}\left(\sin\theta - \sin\theta_s\right)} \\ &= \sum_{n=1}^{m} e^{jnd\frac{\pi}{\lambda}\left(\sin\theta - \sin\theta_1\right)} + \sum_{n=1}^{m} e^{jnd\frac{\pi}{\lambda}\left(\sin\theta - \sin\theta_2\right)} + \ldots \\ &\quad + \sum_{n=1}^{m} e^{jnd\frac{\pi}{\lambda}\left(\sin\theta - \sin\theta_M\right)}, \end{aligned} \tag{5}$$

where $\theta i (i = 1, 2, \ldots, M)$ denotes the main lobe of the ith beam. In Eq. (5), the far-field intensity distribution function is the sum of M different period functions, and θi corresponds to different steering directions, implying that M different main lobes appear at M different positions. Thus, each subarray in Fig. 3(a) is equivalent to an independent small-aperture OPA, which realizes independent scanning of multiple beams, and can detect and improve data acquisition in parallel.

The single-beam high-resolution scanning technique in Fig. 3(b) achieves single-beam scanning by phase-modulating all sub-aperture arrays as a whole. From Eq. (5), it is evident that in the case of a single beam, the array aperture is M times the

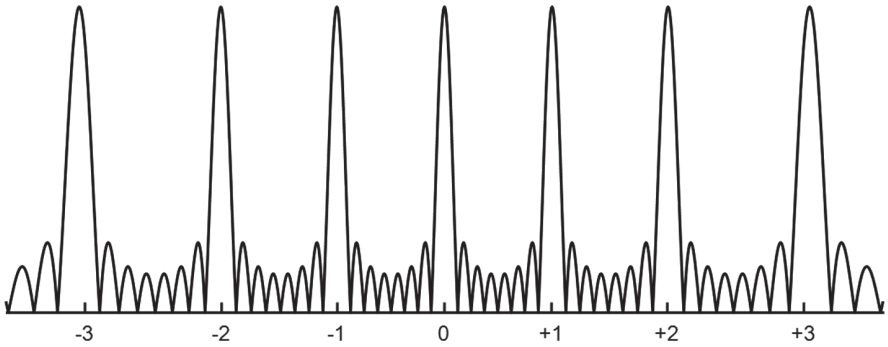

Fig. 2. Schematic diagram of far-field intensity distribution.

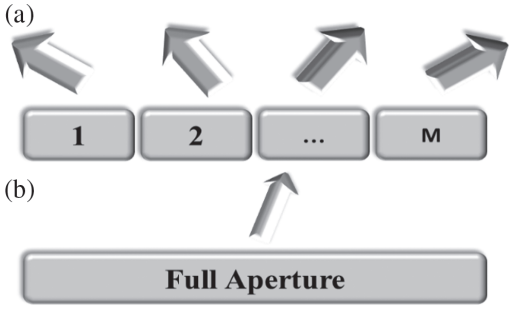

Fig. 3. Schematic of the composite scanning mechanism: (a) sub-aperture multi-beam scanning technique and (b) single-beam high-resolution scanning technique.

sub-aperture, implying that the FWHM of the OPA at this time is $1/M$ that of the multi-beam. Therefore, the single beam has a high-resolution performance and can obtain detailed data in a three-dimensional space. From the above analysis, it is evident that the switching of the two scanning methods can achieve a balance between high resolution and high frame rate, which has excellent potential for practical applications.

The presence of grating lobes in equally spaced phased arrays can interfere with multi-beam scanning, so this paper uses the aperiodic OPA to prevent the appearance of grating lobes. This method destroys the coherence condition of the grating lobe and compresses the energy of grating lobes into the background, which will lead to the enhancement of background noise. Therefore, to design an OPA with good performance, the element spacing must be optimized so that both scanning modes can achieve good grating lobe suppression. Grating lobe suppression refers to obtaining the best sidemode suppression ratio (SMSR):

$$\mathrm{SMSR} = 10\lg\left(\frac{I_{\max\,\mathrm{sidelobe}}}{I_{\mathrm{mainlobe}}}\right), \tag{6}$$

where $I_{\mathrm{maxsidelobe}}$ and I_{mainlobe} represent the maximum-power light of the sidelobe and the power of the main lobe, respectively.

Array optimization is a nonlinear problem, and the SMSR of both the sub- and full aperture must be optimized, which evolves into a multi-objective optimization problem. Here, the multi-objective optimization platform Platemo and the AR-MOEA proposed by Tian *et al.* for the solution are used [18,19]. As shown in Algorithm 1, AR-MOEA uses the same

Algorithm 1. General Framework of AR-MOEA

Input: N (population size), N_R (number of reference points and archive size)
Output: P (final population)
1 $P \leftarrow$ Randomly initialize N solutions;
2 $A \leftarrow P$;
3 $R \leftarrow$ Uniformly generate N_R points on unit simplex;
4 $R' \leftarrow R$;
5 **while** termination criterion not fulfilled **do**
6 $P' \leftarrow$ Select N solutions from P by mating pool selection;
7 $O \leftarrow$ Generate offsprings by genetic operators based on P';
8 $[A, R'] \leftarrow$ Update the archive A and adapted reference points R';
9 $P \leftarrow$ Select N solutions from P by environmental Selection;
10 **end**
11 **return** P;

algorithm framework as most index-based MOEAs. The difference is that AR-MOEA is based on an enhanced inverted generational distance indicator, where a set of points sampled on a unit simplex is adopted as the reference points for calculation of the indicator value. It can adaptively adjust the distribution of the reference points according to the shape of the current population in objective space, and thus make the reference points capable of capturing different shapes of Pareto fronts. The simulation results show that the algorithm is suitable for OPA array optimization. The mathematical model of the array optimization is as follows:

$$\begin{cases} \min\limits_{x} \; f(x) = (f_1(x),\, f_2(x),\, \ldots,\, f_L(x))^T \\ \text{s.t.} \quad \min\,(d_1, d_2, \cdots, d_{N-1}) \geq d_{\min}, \\ \qquad \max\left(d_1, d_2, \ldots, d_{N-1}\right) \geq d_{\max} \end{cases} \tag{7}$$

where $f(x)$ is the SMSR of the optimized target, L is the number of optimization targets, and $d_{\min}$ and $d_{\max}$ are the minimum and maximum spacings between adjacent antennas, respectively. In this experiment, the optimization targets $f(x)$ are the SMSR of the OPA in different cases, such as different angles, various scanning modes, and the difference between beams in the multi-beam case. Considering the size of the optical antenna and the cross talk phenomenon, the optimized range of antenna spacing inside the sub-array is set to $1.3-3.3\lambda$, sub-array spacing is $1.3-9\lambda$, optical wavelength is 1550 nm, total number of OPA elements is 64, number of sub-apertures M is four, and the optimized scanning range is $\pm 40^\circ$.

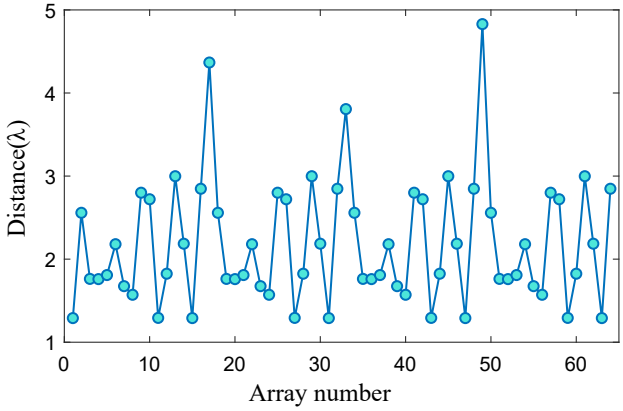

Fig. 4. Array element distribution of the 64-element OPA.

3. SIMULATION

First, consider the simplest case, and assume that the 64-element OPA analyzed is composed of four identical 16-element OPAs. We use the AR-MOEA to optimize the array element spacing of the 16-element OPA and the layout of the four OPAs. The array element distribution of the 64-element OPA obtained is shown in Fig. 4. We use Eq. (1) to calculate the required phase $\Delta\varphi$ for each OPA, and load the phase onto each array element to form the far-field distribution of multiple beams. As shown in Fig. 5(a), the four beams appear at $-30°$, $-10°$, $10°$, and $30°$, respectively. At the same time, we take the 64-element OPA as a whole, and calculate the phase under the full aperture to obtain the far-field intensity distribution of a single beam, as shown in Fig. 5(b). In the multi-beam case, the SMSRs of the four beams are -6.68 dB, and the FWHM values are $1.98°$, $1.87°$, $1.87°$, and $1.98°$, respectively. It can be observed that the SMSR and FWHM of the beam are symmetric about $\theta = 0°$, which is because the four beams can be approximated as one beam formed by the same array at different angles when the sub-apertures are the same. The difference in the energy of the main beam comes from the interaction between the far-field energies of the four sub-arrays. In this case, the result of the symmetry conforms to Eq. (1), and the FWHM of the beam widens with increasing angle. The SMSR is -11.60 dB and the FWHM is $0.36°$ for the single-beam case with $\theta = 0°$, which is approximately 1/4 of the multiple beams. This means that the scanning accuracy of the single beam is about four times that of the multi-beam, and detailed information of the scanned background can be obtained. Further, comparing the beam characteristics in the two scanning modes, it can be observed that the SMSR of the single beam is better than the SMSR of the multi-beam. This is mainly because the sidelobe energies of the subarrays superimpose on each other, leading to an increase in background noise. This deficiency can be solved by subsequent signal processing at the receiving end and increasing the number of array elements, which does not affect the feasibility of the scanning scheme.

Next, the scanning situation of the composite OPA is analyzed. In the multi-beam case, the scanning range of $\pm 40°$ can be evenly divided into four parts. By means of parallel detection, each sub-array is responsible only for the $20°$ field of view to complete the data acquisition of the full field of view, greatly accelerating the efficiency. In addition, compared with the single-beam case, the FWHM of the sub-array is larger, and the number of points collected by scanning the same field of view is less, which can speed up the scanning rate and reduce the subsequent data processing workload. When the object in the field of view is too complex, switching to the single beam with high resolution through phase control does not affect the modeling and analysis of the object. Assume that the multi-beam is rotated $5°$ to the right and the single beam is rotated $40°$ to the right. The required phase $\Delta\varphi$ is calculated for each array element. The obtained far-field intensity distribution is shown in Figs. 5(c) and 5(d). The SMSR of the four beams is -6.05 dB, and the that of the single beam is -11.42 dB, indicating that the variation of SMSR during steering is small. Thus, the designed

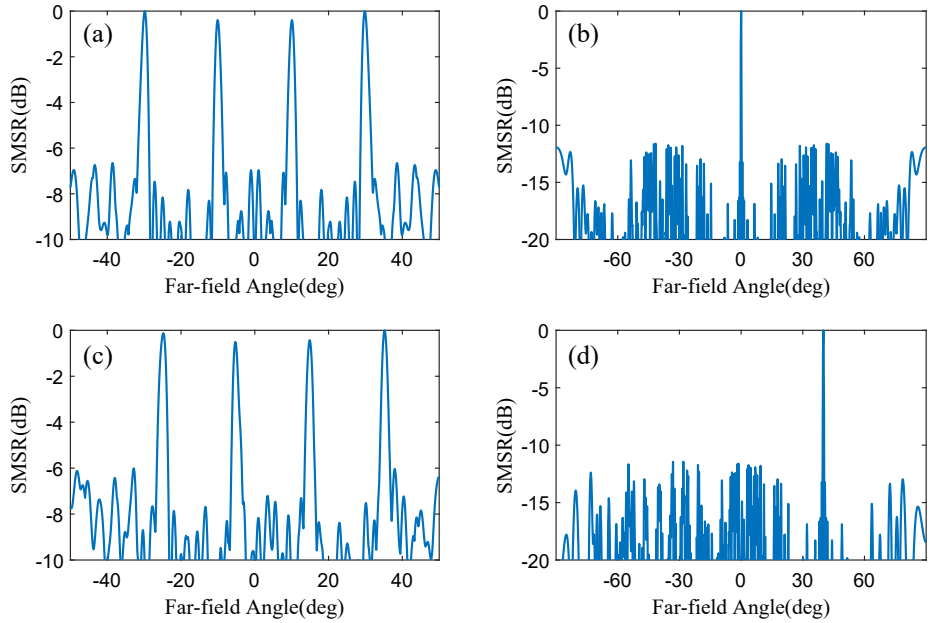

Fig. 5. Far-field intensity distribution: (a) multi-beam; (b) single beam; (c) multi-beam after tunning; (d) single beam after tunning.

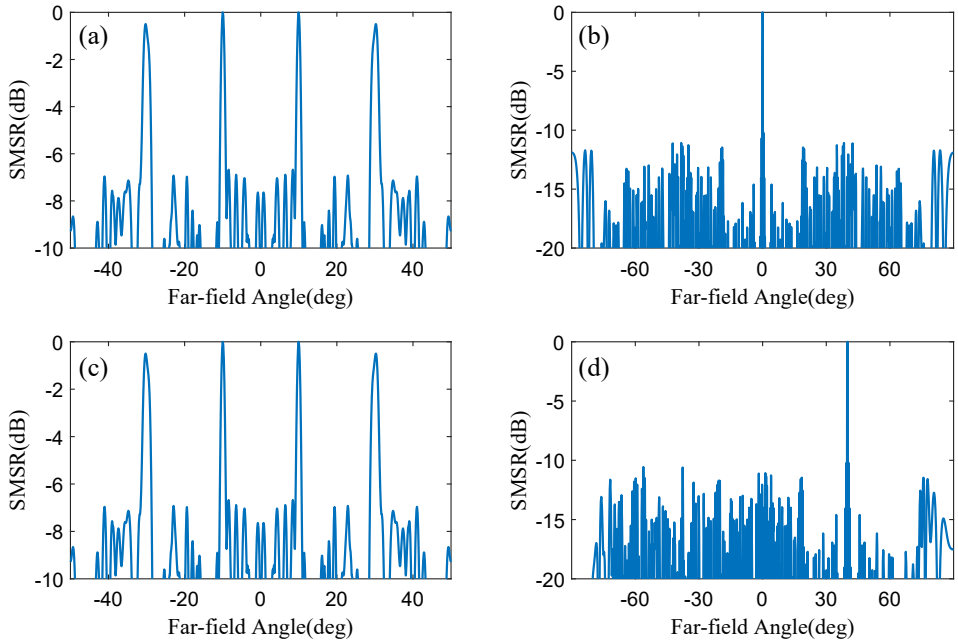

Fig. 6. Far-field intensity distribution: (a) multi-beam; (b) single beam; (c) multi-beam after tunning; (d) single beam after tunning.

OPA also has good scanning characteristics. The above analysis shows that the designed scheme can achieve a balance between high resolution and high frame rate.

Further, the design of a custom array is considered. In practice, we expect different amounts of data and different levels of model precision for different angular ranges within the field of view. Therefore, we need to design the sub-aperture of OPA according to the specific performance requirements in different tasks and environments. For example, we hope that the FWHM of the two beams at $\pm 10°$ is set to 1°, while the FWHM of the two beams at $\pm 30°$ is set to 2°.

Based on the above assumptions, the sub-aperture array of OPA is optimized using AR-MOEA, and the required phase is loaded to obtain the far-field intensity distribution of the OPA, as shown in Fig. 6. In the case of multi-beam, the SMSR is 6.68 dB, the FWHM of the beam is 1.08° at $\theta = \pm 10°$, and the FWHM of the beam is 2.04° at $\theta = \pm 30°$, which is consistent with the design requirements. In the case of single beam, the FWHM is 0.25°, and due to the reduced degrees of freedom for optimization, the SMSR is only 10.22 dB. Similarly, Figs. 6(c) and 6(d) show the far-field intensity distribution after steering, indicating good scanning characteristics of the OPA. It is worth noting that during the optimization process, it was found that the actual FWHM of the multi-beam has an error with the expected results of Eq. (4). We believe this is due to the fact that the far field of the multi-beam is formed by the superposition of the far fields of the four subarrays. Figure 7 shows the individual far-field intensity distribution of the four subarrays. Comparing Figs. 6 and 7, it can be found that the sidelobe energy of the sub-array broadens the main beam and enhances its energy, thus causing the FWHM to be inconsistent with the equation, which brings difficulty to the design. The requirement we assume is relatively simple, but it also shows that the proposed composite scanning scheme has a very high degree of freedom and can be customized to meet different application scenes.

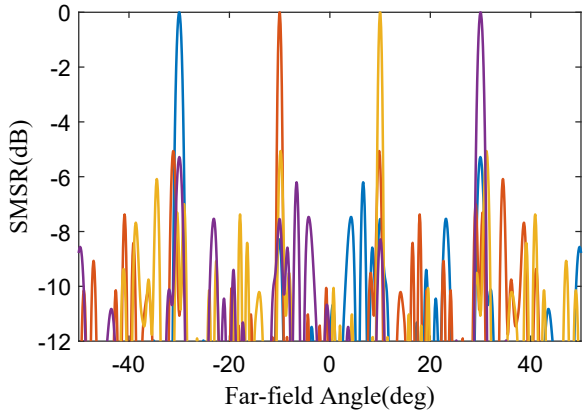

Fig. 7. Individual far-field intensity distributions of the four sub-arrays.

4. CONCLUSIONS

This study proposed a composite scanning technique based on an aperiodic OPA. The OPA of this scheme had two scanning modes, and the scanning mode can achieve adaptive switching according to different environmental conditions. The sub-aperture multi-beam scanning mode realized the scanning of simple objects in the environment more quickly, while the single-beam high-resolution scanning mode obtained detailed information about complex objects. The multi-objective optimization algorithm called AR-MOEA is used to optimize the design of the array element spacing of the aperiodic OPA to achieve grating-lobe suppression. Further, the beam characteristics of the uniform and custom arrays are compared and analyzed through mathematical simulations, which showed that the designed OPA exhibited good performance. The study results provide a new idea for the practical application of OPA in the future.

Funding. Jilin Province Development and Reform Commission (No.2022C046-2).

Acknowledgment. This work is based on PlatEMO, an evolutionary multi-objective optimization platform developed by Anhui University.

Disclosures. The authors declare no conflicts of interest.

Data availability. Data underlying the results presented in this paper are not publicly available at this time but may be obtained from the authors upon reasonable request.

REFERENCES

1. I. Kim, R. J. Martins, J. Jang, T. Badloe, S. Khadir, H. Y. Jung, H. Kim, J. Kim, P. Genevet, and J. Rho, "Nanophotonics for light detection and ranging technology," Nat. Nanotechnol. **16**, 508–524 (2021).
2. X. Sun, L. Zhang, Q. Zhang, and W. Zhang, "Si photonics for practical LiDAR solutions," Appl. Sci. **9**, 4225 (2019).
3. K. Van Acoleyen, W. Bogaerts, J. Jágerská, N. Le Thomas, R. Houdré, and R. Baets, "Off-chip beam steering with a one-dimensional optical phased array on silicon-on-insulator," Opt. Lett. **34**, 1477–1479 (2009).
4. J. Sun, E. Timurdogan, A. Yaacobi, E. S. Hosseini, and M. R. Watts, "Large-scale nanophotonic phased array," Nature **493**, 195–199 (2013).
5. A. Yaacobi, J. Sun, M. Moresco, G. Leake, D. Coolbaugh, and M. R. Watts, "Integrated phased array for wide-angle beam steering," Opt. Lett. **39**, 4575–4578 (2014).
6. C. V. Poulton, M. J. Byrd, P. Russo, E. Timurdogan, M. Khandaker, D. Vermeulen, and M. R. Watts, "Long-range LiDAR and free-space data communication with high-performance optical phased arrays," IEEE J. Sel. Top. Quantum Electron. **25**, 1–8 (2019).
7. C. V. Poulton, A. Yaacobi, D. B. Cole, M. J. Byrd, M. Raval, D. Vermeulen, and M. R. Watts, "Coherent solid-state LIDAR with silicon photonic optical phased arrays," Opt. Lett. **42**, 4091–4094 (2017).
8. K. Wang, A. Nirmalathas, C. Lim, E. Wong, K. Alameh, H. Li, and E. Skafidas, "High-speed indoor optical wireless communication system employing a silicon integrated photonic circuit," Opt. Lett. **43**, 3132–3135 (2018).
9. J. Notaros, C. V. Poulton, M. J. Byrd, M. Raval, and M. R. Watts, "Integrated optical phased arrays for quasi-Bessel-beam generation," Opt. Lett. **42**, 3510–3513 (2017).
10. S. Orfanidis, *Electromagnetic Waves and Antennas* (2014).
11. S. Yin, J. H. Kim, F. Wu, P. Ruffin, and C. Luo, "Ultra-fast speed, low grating lobe optical beam steering using unequally spaced phased array technique," Opt. Commun. **270**, 41–46 (2007).
12. S. Yin, S. Yin, R. Guo, J. H. Kim, J. Yao, P. Ruffin, E. Edwards, C. Brantley, and C. Luo, "Recent advances on multiple channel unequally spaced optical phased array for ultrafast LADAR," Proc. SPIE **7056**, 705619 (2008).
13. K. Chen, Z. He, and C. Han, "A modified real GA for the sparse linear array synthesis with multiple constraints," IEEE Trans. Anntenas Propag. **54**, 2169–2173 (2006).
14. D. Kwong, Y. Zhang, A. Hosseini, and R. Chen, "Integrated optical phased array based large angle beam steering system fabricated on silicon-on-insulator, Proc. SPIE **7943**, 79430Y (2011).
15. T. Komljenovic, R. Helkey, L. Coldren, and J. E. Bowers, "Sparse aperiodic arrays for optical beam forming and LIDAR," Opt. Express **25**, 2511–2528 (2017).
16. D. N. Hutchison, J. Sun, J. K. Doylend, R. Kumar, J. Heck, W. Kim, C. T. Phare, A. Feshali, and H. Rong, "High-resolution aliasing-free optical beam steering," Optica **3**, 887–890 (2016).
17. M. S. Smith, "Phased array fundamentals," in *IEE Tutorial Meeting on Phased Array Radar*, 1989), pp. 1–133.
18. Y. Tian, R. Cheng, X. Zhang, F. Cheng, and Y. Jin, "An indicator-based multiobjective evolutionary algorithm with reference point adaptation for better versatility," IEEE Trans. Evol. Comput. **22**, 609–622 (2018).
19. Y. Tian, R. Cheng, X. Zhang, and Y. Jin, "PlatEMO: a MATLAB platform for evolutionary multi-objective optimization [Educational Forum]," IEEE Comput. Intell. Mag. **12**(4), 73–87 (2017).